Stacking-Fault Enhanced Oxygen Redox in Li₂MnO₃

*Xiang Li, Xinhao Li, Lisa Monluc, Benjamin Chen, Mingxue Tang, Po-Hsiu Chien,
Xuyong Feng, Ivan Hung, Zhehong Gan, Alexander Urban,* and Yan-Yan Hu**

Lattice oxygen redox yields anomalous capacity and can significantly increase the energy density of layered Li-rich transition metal oxide cathodes, garnering tremendous interest. However, the mechanism behind O redox in these cathode materials is still under debate, in part due to the challenges in directly observing O and following associated changes upon electrochemical cycling. Here, with ^{17}O NMR as a direct probe of O activities, it is demonstrated that stacking faults enhance O redox participation compared with Li₂MnO₃ domains without stacking faults. This work is concluded by combining both ex situ and in situ ^{17}O NMR to investigate the evolution of O at 4i, 8j sites from monoclinic *C2/m* and 6c(1), 6c(2), 6c(3) sites from the stacking faults (P3₁12). These measurements are further corroborated and explained by first-principles calculations finding a stabilization effect of stacking faults in delithiated Li₂MnO₃. In situ ^{17}O NMR tracks O activities with temporal resolution and provides a quantitative determination of reversible O redox versus irreversible processes that form short covalent O—O bonds. This work provides valuable insights into the O redox reactions in Li-excess layered cathodes, which may inspire new material design for cathodes with high specific capacity.

1. Introduction

Rechargeable Li-ion batteries (LIBs) are the leading energy storage technology for portable electronics and electric vehicles. The energy density of the present generation of Li-ion batteries is limited by the positive electrode (cathode). Layered manganese (Mn)-based Li-rich cathode materials, with the general formula xLi₂MnO₃•(1-x)LMO₂ with M being the combination of

Ni, Mn, Co, represent state-of-the-art.[1–4] The structure of Li-rich compounds derives from that of layered LiMO₂ (hexagonal cell, space group *R-3m*) by a progressive Li⁺ substitution for M³⁺ and charge compensation with increased valence state of the remaining M elements (M = metal species).[4]

Li-rich materials feature a voltage plateau observed around 4.5 V during the 1st charge process,[4] in which, the initial capacity significantly increases beyond the theoretical transition-metal redox capacity. Many have made the distinction that the participation of lattice O accounts for this extra capacity, at least part of which is attributed to reversible oxidation and reduction of O²⁻ ions in the bulk.[4–6] The exciting prospect of utilizing such reversible oxygen redox to increase the energy density of LIB cathodes has spurred many investigations.[4,5] However, this overcharging beyond the TM redox capacity typically leads to rapid capacity fading and the continuous morphing from a once layered structure during subsequent cycles. Ultimately, these phenomena prevent this class of materials from being broadly commercialized.

O redox participation plays a significant role in the extra capacity of Li excess materials and similar TM containing compounds such as layered sodium transition metal oxides[7–9] and some 4d/5d transition metal oxides.[10–13] Although the electrochemistry of Li-rich materials has been characterized by various techniques, a complete picture of the interplay among structure, composition, and oxygen redox is still elusive. In addition, investigations on the mechanism of oxygen redox will facilitate critical understanding of other anion redox chemistry currently exploited for energy storage and conversion.

Both experimental studies and first-principles density functional theory (DFT) modeling have been employed to provide insights into oxygen redox and structural dynamics. Early work on Li₂MnO₃ and other types of Ni-containing, layered Li-rich materials has shown that lithium intercalation and deintercalation may trigger transition metal (TM) migration and O₂ gas evolution.[11–18] Isotope labeled O₂ gas originating from lattice oxygen was successfully detected by operando gas chromatography-mass spectrometer (GC-MASS).[17] The O redox mechanism was investigated using various techniques that include X-ray photoemission spectroscopy (XPS),[18] soft X-ray absorption (XAS),[19] and electron energy loss spectroscopy.[20] However, the capability of these techniques for probing O valence states

X. Li, L. Monluc, B. Chen, M. Tang, P.-H. Chien, X. Feng, Y.-Y. Hu
Department of Chemistry and Biochemistry
Florida State University
95 Chieftan Way, Tallahassee, FL 32306, USA
E-mail: hu@chem.fsu.edu
X. Li, A. Urban
Department of Chemical Engineering
Columbia University
500 W 120th St, New York, NY 10027, USA
E-mail: au2229@columbia.edu
I. Hung, Z. Gan, Y.-Y. Hu
Center of Interdisciplinary Magnetic Resonance
National High Magnetic Field Laboratory
1800 East Paul Dirac Drive, Tallahassee, FL 32310, USA

is limited by surface sensitivity since it is challenging to disentangle signals from the bulk and the surface. Operando electron paramagnetic resonance (EPR) was employed to determine the TM redox together with an indirect measurement of O redox.[21] High-resolution resonant inelastic X-ray scattering (RIXS) suggested the formation of peroxo-like O—O bonds or hole states on O^{2-}.[19] Moreover, the highly reversible O redox ($\approx$76%) in $Li_{1.17}Ni_{0.21}Co_{0.08}Mn_{0.54}O_2$ was examined by RIXS.[22] Recently, Chueh and co-workers conducted simultaneous RIXS and XAS measurements on Li-rich layered oxides and revealed the relationship between the charge compensation mechanism and structural disorder.[23,24] Based on recent experiments probing atomic vibrations with high resolution, Bruce and co-workers proposed that O_2 molecules can be trapped in the bulk and may be reduced back to lattice O^{2-} upon discharge.[25] On the other hand, first-principles calculations have also identified possible O species with intermediate valence states and their relationship with TM redox.[19,23,24] Computation work indicated the formation of peroxide-like O—O bonds through localized electron holes on oxygen 2p orbitals in some Li-rich cathode materials,[26] leading to unstable oxygen intermediates and eventually molecular O_2.[17] O redox can be promoted by orphaned O 2p states of linear Li–O–Li motifs in Li-rich compositions.[26] Cation defects and electron deficiency have also been argued to be key factors for O redox.[27] Recently, based on their computational studies, Van der Ven and co-workers proposed a two-step oxidation mechanism involving both Mn and O and the formation of a delocalized π-bonded state hybridizing a ring of Mn-d and O-p orbitals.[28,29]

Directly probing O local environments and quantification of lattice O redox activities are a challenge for commonly used techniques. Nuclear magnetic resonance (NMR) has been proved to be a suitable tool for noninvasively determining Li/Na local environments and their evolution during electrochemical operation.[30–32] However, due to large quadrupolar coupling interactions and low natural abundance (0.037%) of NMR-active ^{17}O (spin -5/2) isotope, solid-state ^{17}O NMR shows low sensitivity with poor resolution. ^{17}O-isotope enrichment is often required for sensitivity enhancement. Fast magic-angle-spinning (MAS) or multiple-quantum MAS (MQMAS) NMR experiments at high magnetic fields are usually employed for achieving high resolution. In paramagnetic materials such as transition metal oxide cathode Li_2MnO_3, in addition to the quadrupolar coupling interactions of ^{17}O, interactions between ^{17}O and unpaired electrons in Mn^{4+} serve as another major source to produce very large shift anisotropy and result in overlapping spinning sidebands (SSBs) in ^{17}O NMR spectra, even at ultrafast MAS conditions.[32] Only a few reports are available on paramagnetic ^{17}O NMR studies[33–37] since the 1st paper on ^{17}O NMR was published in 1983.[38] Recently, Grey and co-workers determined the local structures of an ionic-electronic conductor $La_2NiO_{4+\delta}$[31] and pristine cathode Li_2MnO_3[32] using ^{17}O NMR. To obtain high-resolution spectra for reliable assignment and quantification, projection magic-angle-turning phase-adjusted sidebands separation (pjMATPASS)[32] was employed.

In this work, to probe the changes of various O species in Li_2MnO_3, ex situ ^{17}O pjMATPASS NMR was first performed on the ^{17}O-enriched Li_2MnO_3 cathodes at different states of charge. The well-resolved pjMATPASS spectra allow quanti-

fication of different O sites and their redox activities in both the ideal (*C2/m*) and stacking fault (SF, $P3_112$) Li_2MnO_3 structures,[39] respectively. To follow O evolution during the electrochemical cycling, in situ ^{17}O NMR experiments were carried out with the quadrupolar Carr–Purcell–Meiboom–Gill (qCPMG)[40] pulse sequence for enhancement in sensitivity and temporal resolution. To better understand the origin of the experimentally observed varied redox reactivity and reversibility of O sites in Li_2MnO_3 cathodes, DFT calculations were performed on Li_2MnO_3 with different degrees of stacking faults. The combined experimental and theoretical investigation reveals that O at the stacking faults participates more actively in redox reactions with higher reversibility, compared with O sites in stacking fault-free Li_2MnO_3. The enhanced O redox activities at stacking faults are facilitated by stabilized $Li_{2-x}MnO_3$ (SF, $P3_112$) structures.

2. Results and Discussion

2.1. Structural Information

The structure of layered-Li_2MnO_3 with the *C2/m* space group is shown in **Figure 1**a, which can be viewed as an alternating stacking of Li and $Li_{1/3}Mn_{2/3}$ layers along the *c*-axis (Figure 1b). Stacking faults (SFs) often occur along the *c* direction, and stacking of the $Li_{1/3}Mn_{2/3}$ with a *P3_112* space group has been proposed as the model for describing SFs in Li_2MnO_3.[39,41] As seen in Figure 1c,d, the stacking in the ideal Li_2MnO_3 structure[42] is accompanied by an accumulating shift parallel to the cation layers, whereas the SF structure exhibits a threefold screw axis[39,43] that does not give rise to a net lateral shift. O sites in Li_2MnO_3 are all sixfold coordinated with two Mn and four Li atoms in structures with and without stacking faults, however, the Mn–O distance in these octahedral sites differs, which makes them distinguishable via ^{17}O NMR. As seen in Figure 1e–g, a slight adjustment of the Mn–O distance is observed for O sites of SF-Li_2MnO_3 compared with the ideal structure without stacking faults. The Mn–O distance for 6c [1] sites in SF-Li_2MnO_3 becomes asymmetric with a slightly increased average value, compared with O(4i) sites in the SF-free Li_2MnO_3, while the opposite trend is observed for the 6c [2] and 6c [3] sites in the SF-Li_2MnO_3 structure compared with O(8j) sites in SF-free Li_2MnO_3.[32] These changes, albeit small, have a significant impact on O redox and evolution during lithiation and delithiation of SF-Li_2MnO_3, as observed and discussed below. For convenience, O_{4i} and O_{8j} are used to indicate O at 4i and 8j in Li_2MnO_3, respectively, and $O_{SF,6c[1]}$, $O_{SF,6c[2]}$, and $O_{SF,6c[3]}$ are used for the corresponding 6c[1], 6c[2], and 6c[3] sites in SF-Li_2MnO_3 hereafter.

^{17}O NMR can serve as a direct probe to O local structural environments and dynamics. However, ^{17}O NMR is often very challenging due to low sensitivity and low resolution. In this study, sensitivity is enhanced by ^{17}O-isotope enrichment and data acquisition in a high magnetic field of 19.6 T. The spectral resolution of ^{17}O NMR of paramagnetic materials such as Li_2MnO_3 is mainly compromised by anisotropic paramagnetic interactions on the order of MHz including hyperfine and pseudocontact interactions, in addition to chemical shift
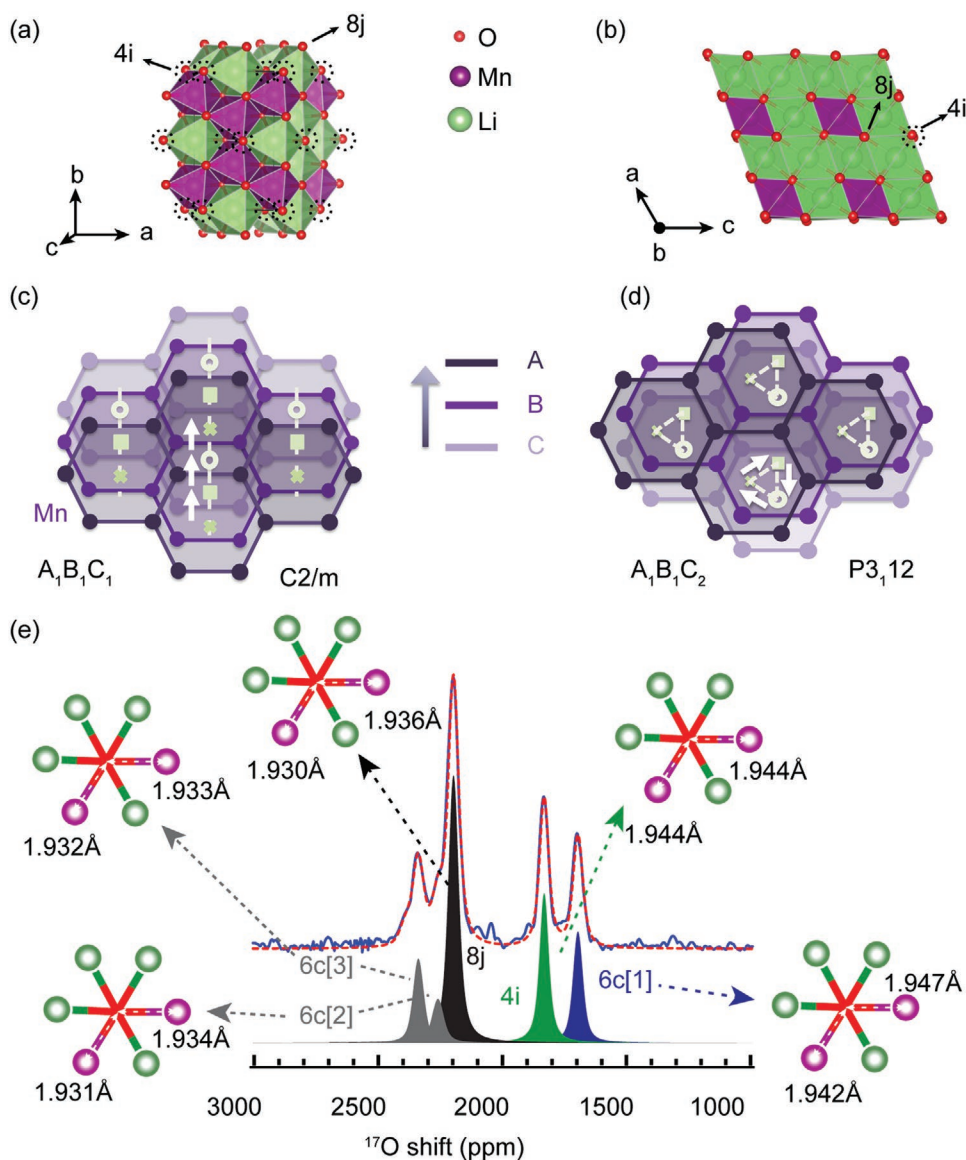
Figure 1. a) Schematic of $Li_{1/3}Mn_{2/3}$ "honeycomb" (001) layer and b) ideal layered structure of Li_2MnO_3. Stacking sequence of the "honey-comb" ($Li_{1/3}Mn_{2/3}$) transition metal (TM) layers in c) ideal and d) stacking-fault (SF-) Li_2MnO_3. e) High-resolution ^{17}O NMR of pristine Li_2MnO_3. O coordination environments and bond lengths of O at 6c(1), 6c(2), 6c(3) sites (SF-Li_2MnO_3, space group: $P3_112$) and 8j, 4i sites (ideal Li_2MnO_3, space group: $C2/m$) are also shown.

anisotropy and quadrupolar interactions, resulting in extremely broad peaks shifted far away from 0 ppm. As shown on top of the 2D spectrum in Figure S1a of the Supporting Information, the ^{17}O MAS NMR of Li_2MnO_3 acquired with a stimulated echo method presents a spectrum spanning over 4000 ppm. The large shift anisotropy, manifested as manifolds of SSBs overlapping with isotropic peaks, is due to strong paramagnetic interactions between unpaired electrons from transition metal Mn^{4+} ions and ^{17}O nuclear spins. To achieve the highest resolution for site identification and quantification, the pjMATPASS[32] technique is applied to separate different orders of SSBs. Spectral shearing along the F2 dimension aligns all SSBs at their isotropic positions and the projection presents the purely isotropic spectrum with significantly enhanced sensitivity

(Figure S1b, Supporting Information; Figure 1e). Five ^{17}O NMR peaks are resolved, resonating at 1700, 1840, 2180, 2280, and 2340 ppm, respectively. These are attributed to two different O structural environments in Li_2MnO_3 and three in SF-Li_2MnO_3 as discussed above. ^{17}O NMR shifts are mainly determined by the hyperfine interactions between the unpaired electron spins of Mn^{4+} and ^{17}O nuclear spins, which are thus very sensitive to Mn–O distance. Shorter averaged Mn–O distances in this case will yield stronger hyperfine interactions, thus larger shifts of the resonances from 0 ppm. Therefore, based on the analysis of the Mn–O distances (Figure 1e) in Li_2MnO_3 structures with and without stacking faults, the resonances at 1840 and 2180 ppm are assigned to O_{4i} and O_{8j}, respectively, and resonances at 1700, 2280, and 2340 ppm are from $O_{SF,6c[1]}$, $O_{SF,6c[2]}$, and

**ADVANCED
SCIENCE NEWS**

www.advancedsciencenews.com
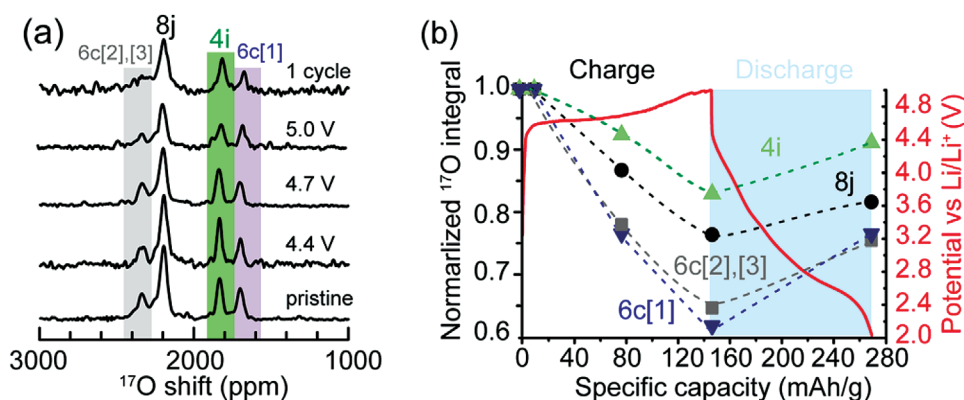
**ADVANCED
ENERGY
MATERIALS**

www.advenergymat.de

Figure 2. Evolution of various O sites in Li_2MnO_3 upon electrochemical cycling probed by high-resolution ^{17}O NMR. a) High-resolution ^{17}O NMR spectra of Li_2MnO_3 electrodes at different states of charge, revealing changes of O sites with electrochemical cycling. b) The corresponding normalized quantification based on spectral areal integrals, along with the electrochemical profile.

$O_{SF,6c[3]}$, respectively.[32] With the signatures of various O sites in Li_2MnO_3 identified in ^{17}O NMR, it is possible to follow the evolution of different O local environments in Li_2MnO_3 upon electrochemical cycling.

2.2. Ex Situ ^{17}O NMR of Li_2MnO_3 at Different States of Charge

To follow redox activities of different O sites in Li_2MnO_3 upon electrochemical cycling, ^{17}O pjMATPASS NMR is performed on Li_2MnO_3 cathodes charged to 4.4, 4.7, and 5.0 V, together with one discharged to 2.0 V. These representative states are chosen for the following reasons: complete oxidation of residual Mn^{3+} to Mn^{4+} occurs at 4.4 V; the quasi-plateau accompanied with O redox ends at 4.7 V, and top of charge is at 5 V. As shown in **Figure 2**, upon charge, all the peaks in the ^{17}O NMR spectra become much broader, suggesting increased structural disorder upon cycling. All O NMR resonances exhibit decreased areal integral, and among them, the reduction in $O_{SF,6c[1]}$, $O_{SF,6c[2]}$, and $O_{SF,6c[3]}$ resonances is most prominent, up to 37.2% at the top of the charge. In comparison, the reduction of the O_{4i} and O_{8j} NMR resonances is less than their counterparts in SF-Li_2MnO_3, i.e., O_{4i} versus $O_{SF,6c[1]}$, and O_{8j} versus $O_{SF,6c[2]}$ and $O_{SF,6c[3]}$. In addition, the O sites with shorter Mn–O distances (O_{8j}) see more decrease in ^{17}O NMR than those with longer Mn–O distances (O_{4i}). Upon discharge, the intensity of ^{17}O resonances increases but does not fully recover to their pristine states. Quantitative analysis is carried out based on the areal integral of each ^{17}O resonance. Upon charge to 4.4 V, O at all sites remains nearly constant. This short period is mainly related to the oxidation of residual Mn^{3+} to Mn^{4+}. From 4.4 to 5.0 V, the signal of all O sites decreases significantly, which is attributed to O^{2-} oxidation, accounting for the extra capacity as commonly perceived.[12–14] Between 4.4 and 5.0 V, $O_{SF,6c[1]}$, $O_{SF,6c[2]}$, and $O_{SF,6c[3]}$ show similar and faster decay compared to O_{4i} and O_{8j}, indicating O at these stacking faults is more active. It is worth noting that a minor ^{17}O component (Figure S2, Supporting Information) at ≈1700 ppm shows up at 5 V but disappears upon lithiation, the origin of which is not clear. Upon discharge, partial recovery of ^{17}O NMR signal loss for O_{4i}, O_{8j}, and $O_{SF,6c}$ sites is observed. Compared to the O amount in the

pristine sample before electrochemical cycling, at the end of the first charge–discharge cycle, O_{4i} recovers to 91.6%, O_{8j} to 82.0%, and $O_{SF,6c}$ to 75.8%. To evaluate the reversibility of O redox activity, only participating O sites should be considered. For instance, the participating O_{8j} is ≈23.2% and the recovered O_{8j} is 5.2% of total O_{8j}, thus the O_{8j} redox reversibility is 5.2%/23.2% = 22.4%. Compared with O_{8j}, O_{4i} has a lower participation rate of 16.4% but the recovery is ≈8.0% of the total O_{4i}, thus the redox reversibility is 8.0%/16.4% = 48.8%. This may be because O_{8j} locates within Mn-concentrated domains with shorter Mn–O distances while O_{4i} resides within Li domains with longer Mn–O distances. Electron delocalization may occur between Mn and O_{8j}, thus Mn redox likely activates and destabilizes O_{8j}.[28,29] For the corresponding SF sites, i.e., $O_{SF,6c[1]}$ and $O_{SF,6c[2,3]}$, the redox reversibility is 13.9%/37.2% = 37.4% and 10.5%/34.6% = 30.3%, respectively. The $O_{SF,6c}$ sites exhibit both relatively high O redox activity and reversibility.

2.3. Stacking Faults and Their Stabilization Effects

2.3.1. Quantification of Stacking Faults with Ex Situ ^{17}O NMR

In light of the finding that O in SF-Li_2MnO_3 more actively participates in O redox, Li_2MnO_3 with different amounts of stacking faults are prepared and further investigated. The fraction of stacking faults in Li_2MnO_3 is known to depend on the synthesis temperature. Lower calcination temperature introduces more structural defects of $Li_{1/3}Mn_{2/3}$ planes along the c-axis, which has been well characterized by diffraction methods.[39,41,43] Li_2MnO_3 with different degrees of stacking faults are synthesized at 700 and 900 °C, respectively. **Figure 3**a shows the 1st charge–discharge profiles of a Li_2MnO_3/Li battery. Lower annealing temperature at 700 °C delivers a charge capacity of 145 mAh g^{-1} and a discharge capacity of 124 mAh g^{-1}, corresponding to ≈0.63 Li removal and 0.54 Li reinsertion and a coulombic efficiency of 86%. By contrast, Li_2MnO_3 prepared at 900 °C only shows a charge capacity of 101 mAh g^{-1} and a discharge capacity of 66 mAh g^{-1}, yielding a coulombic efficiency of 65%. The additional capacity obtained in the 700 °C-sample upon charge occurs mainly near 4.5 V, which is associated with
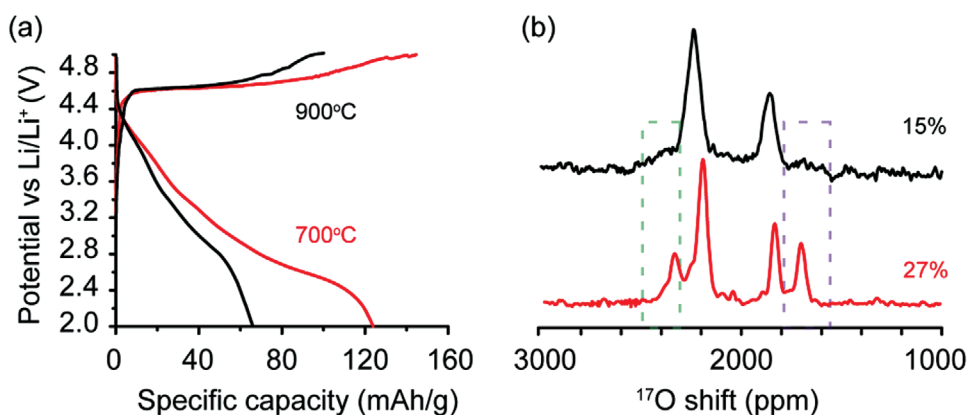
**ADVANCED
SCIENCE NEWS**

www.advancedsciencenews.com

**ADVANCED
ENERGY
MATERIALS**

www.advenergymat.de

Figure 3. Comparison of the a) electrochemical profiles and b) ^{17}O NMR spectra of Li_2MnO_3 prepared at 700 °C (red) and 900 °C (black), respectively. The O at% within SFs, 15% versus 27%, shown in (b) are calculated based on the peak areal integrals of the corresponding ^{17}O NMR resonances for $O_{SF,6c[1,2,3]}$, as marked with the dashed rectangle, over the total spectral areal integrals.

O redox processes. The amount of stacking faults in these two samples is quantified with high-resolution ^{17}O NMR as shown in Figure 3b. Based on the areal integrals of the ^{17}O NMR resonances, O_{6c}[1], [2], and [3], and total spectral areal integral, the fraction of stacking faults is 27% in the sample prepared at 700 °C, compared with 15% for the sample prepared at 900 °C. These results further suggest that stacking faults promote O redox in Li_2MnO_3.

2.3.2. Stabilization Effects of Stacking Faults Revealed by DFT Calculations

To better understand the impact of SFs on the redox mechanism, we performed a computational delithiation of ideal and SF-Li_2MnO_3 structure models using DFT calculations as detailed in the Experimental Section. The SF-Li_2MnO_3 structure model with space group $P3_112$ was constructed using a reference.[39] The stacking sequence of the $Li_{1/3}Mn_{2/3}$ layers in both structures is schematically shown in Figure 1c,d and the

atomic structures are displayed in Figure S3 of the Supporting Information.

Figure 4a shows an analysis of the relative formation energies of the ideal and SF-Li_2MnO_3 structures. The formation energy of SF-Li_2MnO_3 is only 1.6 meV/Li_2MnO_3 above the ideal structure. This small energy difference is in good agreement with the high SF concentration found in the experiment (Figure 3). As seen in Figure 4a, the SF-Li_2MnO_3 structure is energetically preferred for intermediate Li contents, as implied by lower formation energies compared with ideal Li_2MnO_3 for $x < 1.86$ in $Li_{2-x}MnO_3$. This stabilization can be attributed to a distortion that the structure undergoes when Li is extracted from the $Li_{1/3}Mn_{2/3}$ layer. The neighboring (vacancy$_{1/3}$Mn$_{2/3}$) planes shift relative to each other such that the Li vacancies are exactly aligned in the direction of the c-lattice vector. This local distortion creates highly stable Li sites in the Li layer that are only coordinated by vacancies and not by any cations (Figure S4, Supporting Information). Such a distortion is not possible in the ideal Li_2MnO_3 structure because of the lateral translation of the $Li_{1/3}Mn_{2/3}$ planes (Figure 1c). To further
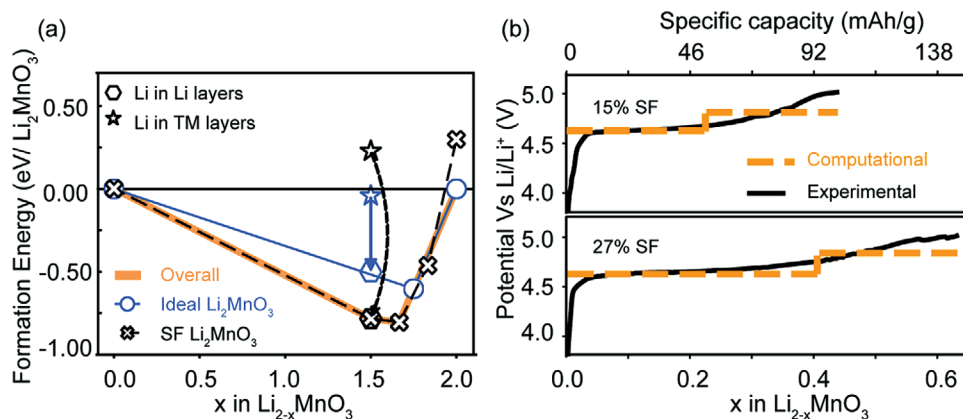

Figure 4. a) Formation energy convex hull construction predicted by SCAN+rVV10+U calculations including configurations based on the ideal Li_2MnO_3 structure (blue circles and solid line) and the stacking-fault (SF-) Li_2MnO_3 structure (black crosses and dashed line). The overall convex hull based on both ideal and SF structures is highlighted with a thick orange line. Arrows indicate the energy difference between structures in which the Li sites within the Mn layer are occupied (star symbols) and those in which the Li atom has migrated to the Li layer (hexagon symbols). b) Calculated voltage profiles as predicted by SCAN+rvv10+U calculations for Li extraction from Li_2MnO_3 with the two different stacking-fault concentrations seen in NMR, 15% and 27%, respectively. Experimental voltage profiles of Li_2MnO_3 prepared at 900 and 700 °C are plotted as a reference.

quantify the stabilization associated with the distortion of the SF structures, the energy differences between structures with a Li atom in the $Li_{1/3}Mn_{2/3}$ and with Li vacancies in the $Li_{1/3}Mn_{2/3}$ plane are indicated by arrows in Figure 4a.

Due to the stabilizing effect of SFs for delithiation, deeper delithiation can be induced in SF-Li_2MnO_3 upon charge at relatively low voltages compared with ideal Li_2MnO_3, yielding additional capacity. Figure S5 of the Supporting Information shows the equilibrium voltage profiles calculated from the formation energies of Figure 4a. The potential for Li extraction from the SF structure is ≈0.2 V lower than that for Li extraction from the ideal Li_2MnO_3 structure until 1.5 Li have been extracted, which means that delithiation occurs first at the stacking faults (plateau at ≈4.6 V in the calculated profiles). The ideal Li_2MnO_3 domains start to be delithiated only after 75% Li has been extracted from the SF domains of the material. Figure 4b shows the calculated equilibrium voltage profiles for the two Li_2MnO_3 with different SF concentrations characterized above (Figure 3b). As seen in Figure 4b, the predicted length of the low-voltage (SF) plateau is in excellent agreement with the experimental voltage profiles and corresponds to the additional charge capacity that is observed with increasing SF concentration. Deeper delithiation of SF-Li_2MnO_3 requires commensurate oxidation of O^{2-}, echoing with the observed increased O redox activities in SF-Li_2MnO_3.[40]

The structural motifs that form upon delithiation of ideal and SF-Li_2MnO_3 are shown in Figures S6 and S7 of the Supporting Information. As seen in the figures, our calculations predict that oxygen oxidation leads to the formation of O—O ("peroxo") bonds and, as a consequence, the closure of the Li layer from initially ≈2.6 Å to only ≈1.4 Å. Such a collapse of the interslab distance is a known degradation mechanism in other layered cathode materials,[44,45] and is likely irreversible also in Li_2MnO_3, leading to capacity loss.

We note that our results for the ideal Li_2MnO_3 are consistent with previous computational work. Van der Ven and co-workers reported the delithiation phase diagram of Li_2MnO_3 both assuming static Mn and assuming Mn migration.[29,46] We investigated partial delithiation during the first charge and our NMR measurements did not show evidence for Mn migration, therefore the static Mn case became relevant. Xiao et al. also investigated Li extraction from Li_2MnO_3 using DFT and lattice model simulations choosing half-delithiated Li_1MnO_3 as a formation-energy reference,[47] however, both our calculations as well as other computational studies[29,46,47] predict this composition to be thermodynamically unstable.

2.4. Tracking O Activities with In Situ ^{17}O NMR

The combination of high-resolution ^{17}O NMR and computation has shed new light on the origin of excess capacity observed in Li_2MnO_3, showing that O redox is facilitated by deeper delithiation within the domains of stacking faults. To track O redox closely in Li_2MnO_3 cathodes upon charge and discharge against Li anodes, in situ ^{17}O NMR is employed to monitor the O local structural changes in real time during electrochemical cycling. To enhance the sensitivity and ensure broad spectral excitation, in addition to [17]O-enrichment of the Li_2MnO_3 electrodes

at 850 °C, in situ ^{17}O NMR was acquired using the qCPMG[40] method at a high magnetic field (19.6T). It is worth noting that the temporal resolution in an in situ acquisition is gained with the sacrifice of spectral resolution due to the challenges associated with spinning the battery cell. The in situ static ^{17}O NMR spectrum of a pristine Li_2MnO_3/Li cell is shown in **Figure 5**a; three resonances can be partially resolved, assigned to solid-electrolyte interphase (SEI, 0 ppm), 4i/6c[1] (centered around 1700 ppm), and 8j/6c[2,3] (centered around 2200 ppm) sites, respectively. The SEI component accounts for 0.8% of total O and grows with cycling up to 1.5%. The intensity of the [17]O resonances from Li_2MnO_3 oscillates following the charge and discharge processes.

The full set of the in situ ^{17}O NMR spectra on a Li_2MnO_3/Li cell over the first two charge–discharge cycles and detailed quantitative analysis results are displayed in Figure 5b,c, and Figure S8 (Supporting Information), along with the corresponding electrochemical profile. During the 1st charge, 0.22 Li is extracted per Li_2MnO_3 unit and 0.12 Li is reintercalated upon discharge. In the 2nd cycle, 0.31 Li is extracted from Li_2MnO_3 and 0.22 Li is reintercalated. Increased capacity following the 1st activation cycle was also observed for Li_2MnO_3 in previous reports.[21,48] The specific capacity obtained here is not optimized to the best reported values in the literature due to the limitation of the battery cell containers required for the in situ NMR characterizations. Nevertheless, the in situ studies provide additional insights beyond the conclusions drawn from ex situ characterizations and the nondestructive nature of the experimental setup affords reliable quantitative analysis.

At the beginning of the charge, only a small amount of 0.01 Li is extracted below 4 V, accompanied by the oxidation of residual $Mn^{3+} \rightarrow Mn^{4+}$, echoing with our previous operando EPR studies on Li_2MnO_3.[21] This result is also in good agreement with the expectations since the Mn ions are formally in a 4+ oxidation state in pristine Li_2MnO_3. Upon further delithiation to 4.5 V, the electronic structure of Li_2MnO_3 continues to exhibit similar features as $Na_2Mn_3O_7$[24,28,29,49] and has the same symmetry and energy-level splitting behavior as the π(Mn–O) process in $Na_2Mn_3O_7$[28] Electrons are likely extracted from the delocalized π(Mn–O) system of Mn-d and O-p orbitals, echoing with the increase in Mn valence states observed from operando EPR.[21] By contrast to $Na_2Mn_3O_7$, the π-systems in the Mn_6-rings of Li_2MnO_3 overlap,[29] the voltage of the π-redox increases to 4.7–4.8 V once more Li is extracted, which is accompanied by oxygen redox participation, i.e., O^{2-} oxidizes to form O_2^{n-} (n = 3, 2, 1, and/or 0), explaining the absence of changes observed on Mn in our operando EPR studies.[21] A previous ex situ investigation showed that O_2^{2-} does not readily form for Mn-based cathodes.[17] O_2^{n-} is strongly paramagnetic when $n = 1$ and 3, which will render O_2^{n-} likely unobservable in ^{17}O NMR and also cause fast relaxation of [17]O magnetization from surrounding O^{2-}, due to strong coupling between unpaired electrons in O_2^{n-} and nearby [17]O nuclear spins. Accordingly, as seen in Figure 5c, a gradual decrease in ^{17}O NMR signal is observed between 4 and 4.5 V, especially around 4.5 V, corresponding to π(Mn–O) redox. This is followed by a slightly steeper decrease in the ^{17}O NMR signal, due to both O^{2-} loss and the yielded paramagnetism. With Li reintercalation upon discharge, electrons are injected into the π(Mn–O) system, resulting in an increased
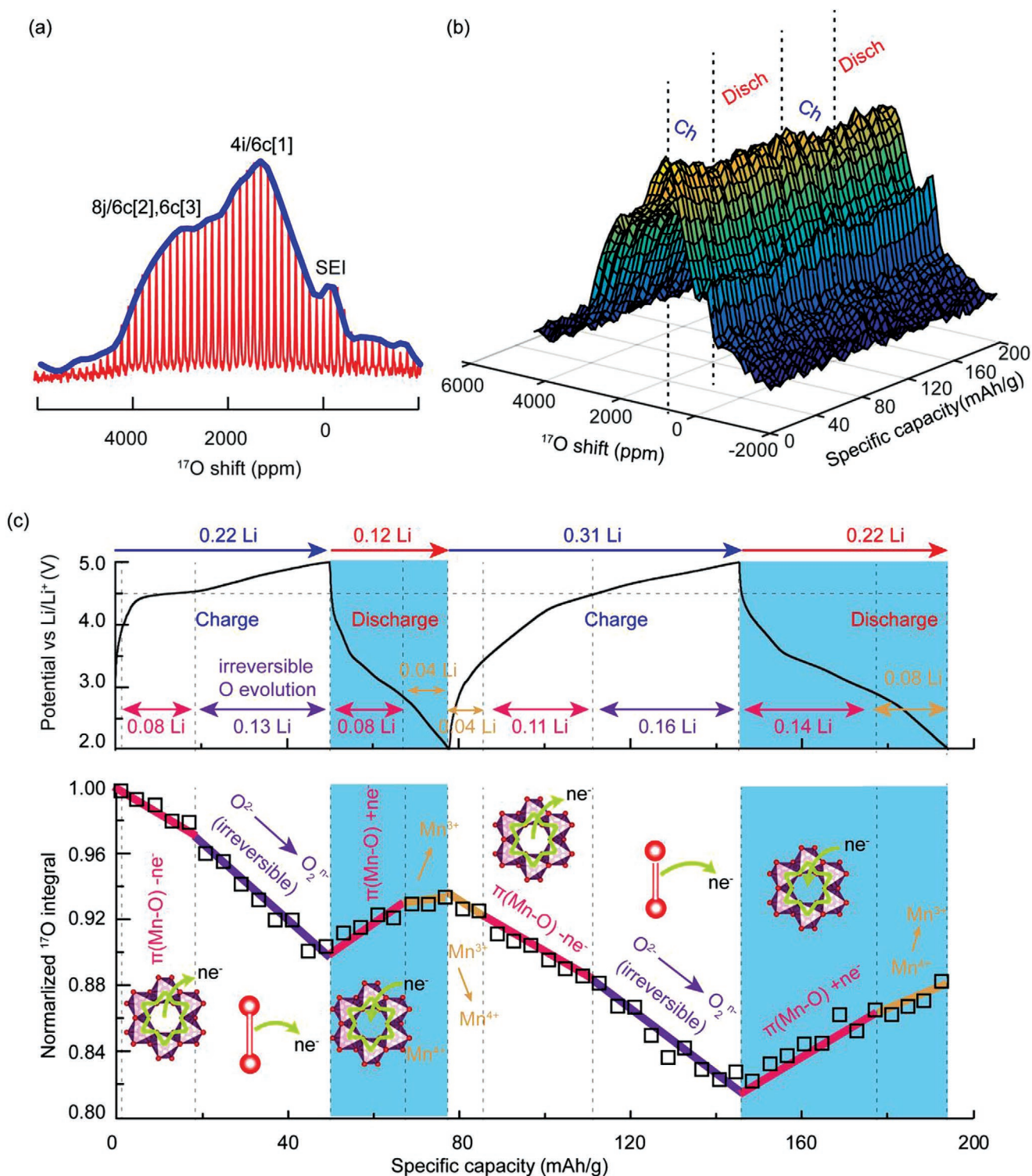
Figure 5. a) In situ ^{17}O NMR for tracking O activities in Li_2MnO_3. ^{17}O static CPMG NMR spectrum of a Li_2MnO_3/Li half-cell battery before cycling. b) The full set of the in situ ^{17}O NMR spectra of the same Li_2MnO_3/Li half-cell battery as a function of specific capacity. c) Quantification of total ^{17}O NMR signal from the Li_2MnO_3 cathode during cycling and the proposed redox mechanism based on areal integrals of the in situ ^{17}O NMR spectra shown in (b) and operando EPR.[21]

^{17}O NMR signal and a decreased Mn^{4+} seen in EPR.[21] Below 4.0 V, Mn^{4+} ions are reduced to Mn^{3+}, and an increased ^{17}O NMR signal is observed at the end of discharge. The total irreversible

loss of ^{17}O NMR signal after the first cycle is nearly 7%. At the beginning of the 2nd charging process, Mn^{3+} is first oxidized to Mn^{4+} from 2.0 to 4.0 V followed by electron extraction from

the π(Mn–O) system, both of which reduce the ^{17}O NMR signal. The high potential near the top of charge again promotes O^{2-} oxidation to form O_2^{n-}, leading to a steeper decrease in the ^{17}O NMR signal. The 2nd discharge shows a similar trend as the 1st discharge. However, due to the activation process of the 1st cycle, a higher specific capacity is observed for the 2nd cycle, which is attributed to reversible π(Mn–O) and $Mn^{3+/4+}$ redox. Another 5% total loss in ^{17}O NMR signal is seen at the end of the 2nd charge–discharge cycle, due to irreversible O redox, i.e., O_2 evolution and SEI formation which transfers ^{17}O from paramagnetic Li_2MnO_3 to diamagnetic oxides. Overall, the in situ ^{17}O NMR combined with prior operando EPR studies[21] reveal that reversible O redox in Li_2MnO_3 requires at least apparent participation of Mn, maybe via the formation of π(Mn–O) complex involving Mn-d and O-p orbitals. It is worth noting that this does not eliminate the possibility of a two-step oxidation mechanism, involving individual oxidation of O or Mn first followed by fast ($>10^{-10}$ s^{-1}) consolidation of electrons in the delocalized π(Mn–O) system.

3. Conclusion

The O activity in Li_2MnO_3 cathodes during electrochemical cycling is directly probed using high-resolution and in situ ^{17}O NMR. Different O sites in Li_2MnO_3 with and without stacking faults have been identified and quantified, and their redox processes are monitored. O in SF-Li_2MnO_3 participates more actively in redox reactions compared with O in SF-free Li_2MnO_3. First-principles calculations unveiled that stacking faults stabilize partially delithiated-Li_2MnO_3, leading to deeper delithiation of SF-Li_2MnO_3 at lower charging potential compared with SF-free Li_2MnO_3, consistent with the experimental findings. Deeper delithiation increases the amount of O participating in the redox reactions. Aggressive delithiation of SF-$Li_{2-x}MnO_3$ beyond $x > 1.75$ in SF domains leads to irreversible formation of peroxo O—O bond. In addition, in situ ^{17}O NMR closely tracks O activities with an improved temporal resolution, which helps quantify reversible O redox reactions involving the π(Mn–O) complex with delocalized electrons, irreversible O—O bond formation, and SEI formation. Since the O redox mechanism in high-voltage cathodes is still under debate, ^{17}O NMR provides useful information about the redox activity of different O sites and allows discerning reversible from irreversible O redox. In addition, the gained insights, especially the promotion of O redox participation by stacking faults via stabilization effects, point toward new strategies for activating anion redox in Li-cathodes.

4. Experimental Section

Synthesis of Li₂MnO₃: Li_2MnO_3 was synthesized using a solid-state reaction method from precursors LiOH and $MnCO_3$ with a molar ratio of LiOH:$MnCO_3$ = 2.05:1.00. The mixture of the precursors was first ball-milled for 1 h, followed by calcination at 700 °C for 24 h.

¹⁷O-Isotope Enrichment: The ^{17}O-enrichment of the as-synthesized L_2MnO_3 was first dried at 500 °C for 12 h. About 120 mg dried Li_2MnO_3 powder was placed in a closed quartz tube filled with 70% $^{17}O_2$ (Cambridge Isotope Laboratories) and then heated at 850 °C for 24 h

to facilitate ^{17}O–^{16}O isotope exchange. The closed quartz tube with the enriched sample was naturally cooled down to room temperature before the ^{17}O-enriched powder was harvested.

X-Ray Diffraction Characterization: The crystal structures of Li_2MnO_3 were determined by X-ray diffraction using a diffractometer (X'PERT Pro MPD, Cu Kα radiation, λ = 0.15406 nm). The diffraction patterns were recorded at room temperature in the 2θ range from 10° to 80°, with a scan rate of 7° min^{-1}.

Battery Fabrication and Electrochemical Cycling: The synthesized Li_2MnO_3 was mixed with polyvinylidene fluoride (Kynar Flex 2801 from Arkema) and conductive acetylene black (80 wt:10 wt:10 wt). The mixture was dispersed in N-methyl-2-pyrrolidone and manually ground in an agate mortar for 30 min to form a homogenous slurry. The slurry was cast onto Al foil and Ti mesh to make cathodes for coin cells and in situ bag cells, respectively. The cathodes were dried at 120 °C for 4 h under vacuum before being assembled into the batteries in an Argon-filled glovebox. In the assembled Li-ion CR2032 coin cells, the Li_2MnO_3 cathode and Li metal anode were separated by a piece of porous glass microfiber (Whatman, type GF/D) soaked with LP30 electrolyte which contains 1 M LiPF$_6$ in ethylene carbonate and dimethyl carbonate (1:1, W/W, Merck). The cells were cycled on LAND within a voltage window of 2–5 V.

Ex Situ ¹⁷O NMR: ^{17}O MAS solid-state NMR experiments were performed on a Bruker Avance I spectrometer in a 19.6 T magnetic field at a ^{17}O Larmor frequency of 112.57 MHz. Samples at different states of charge were packed into 3.2 mm rotors and spun at 18 kHz. The magic-angle turning and phase-adjusted sidebands (MATPASS) pulse sequence was employed to achieve well-resolved NMR spectra for Li_2MnO_3.[32] The recycle delay was 0.1 s and the 90° pulse length was 0.8 μs. All ^{17}O chemical shifts are referenced to liquid H_2O at 0 ppm.

In Situ ¹⁷O NMR: For in situ ^{17}O NMR measurements, plastic bag-cell batteries were assembled in an argon-filled glovebox and placed inside a home-built static NMR probe. ^{17}O NMR spectra were collected while the batteries were cycled at a rate of C/50, with the theoretical capacity C = 458 mAh g^{-1} (assuming all Li ions are completely extracted) used for Li_2MnO_3. All in situ ^{17}O NMR acquisitions were carried out on a Bruker Avance I spectrometer in a 19.6 T magnetic field with a ^{17}O Larmor frequency of 112.57 MHz. The ^{17}O spectra were obtained using a qCPMG sequence for both broadband excitation and enhanced sensitivity. A 90° pulse length of 1.56 μs was used with a recycle delay of 0.4 s. The transmission frequency (SFO1) was set at 2000 ppm. Spectra were processed and analyzed by using Topspin (version 3.5) and Matlab (version R2014b). Matlab codes were developed for simulating qCPMG spectra and performing spectral areal integration.

First-Principles Calculations: DFT calculations were performed using the Vienna Ab initio simulation package[50,51] with projector augmented-wave pseudopotentials[52,53] using the spin-polarized generalized gradient approximation (GGA) by Perdew, Burke, and Ernzerhof (PBE).[54] The electronic wave functions were represented in a plane-wave basis set with an energy cutoff of 520 eV. The strong correlation of Mn d electrons was addressed with a rotationally invariant Hubbard U correction.[55] A Hubbard-U parameter of U = 3.9 eV, previously determined by Jain et al.,[56] was used. Γ-centered k-point meshes with $N_i = \left[\max(1, 25 \mid \vec{b}_i \mid)\right]$ points in reciprocal direction i were used for the integration of the Brillouin zone, where $\vec{b}_i$ is the ith reciprocal lattice vector. Self-consistent field calculations used Gaussian smearing of width 0.05 eV and an energy convergence criterion of 10^{-5} eV. The convergence thresholds for atomic forces in geometry optimizations was 10^{-4} eV Å^{-1}. Delithiated Li_xMnO_2 configurations of the ideal and stacking-fault structures were obtained from systematic enumeration of lithium-vacancy orderings in cell sizes based on 4 and 6 Li_2MnO_3 formula units, respectively. The results obtained from PBE+U calculations were followed by single-point calculations using the SCAN+rVV10+U meta-GGA functional[57,58] with U = 2.7 eV[59] to achieve a more accurate estimate of the impact of oxygen redox, and all data reported in the main manuscript were obtained from SCAN calculations. All input files for DFT calculations and the convex hull constructions were generated using the Python Materials Genomics (pymatgen) toolkit.[55,60] Lithium-vacancy orderings

were enumerated using the library and methods by Hart et al.[61–63] as interfaced with pymatgen.

Supporting Information

Supporting Information is available from the Wiley Online Library or from the author.

Conflict of Interest

The authors declare no conflict of interest.

Data Availability Statement

The data that support the findings of this study are available in the supplementary material of this article.

[1] D. Larcher, J.-M. Tarascon, *Nat. Chem.* **2015**, *7*, 19.

[2] S. Rothermel, M. Evertz, J. Kasnatscheew, X. Qi, M. Grützke, M. Winter, S. Nowak, *ChemSusChem* **2016**, *9*, 3473.

[3] A. Manthiram, J. C. Knight, S.-T. Myung, S.-M. Oh, Y.-K. Sun, *Adv. Energy Mater.* **2016**, *6*, 1501010.

[4] P. Rozier, J. M. Tarascon, *J. Electrochem. Soc.* **2015**, *162*, A2490.

[5] E. Lee, K. A. Persson, *Adv. Energy Mater.* **2014**, *4*, 1400498.

[6] Y. Shin, H. Ding, K. A. Persson, *Chem. Mater.* **2016**, *28*, 2081.

[7] U. Maitra, R. A. House, J. W. Somerville, N. Tapia-Ruiz, J. G. Lozano, N. Guerrini, R. Hao, K. Luo, L. Jin, M. A. Pérez-Osorio, F. Massel, D. M. Pickup, S. Ramos, X. Lu, D. E. McNally, A. V. Chadwick, F. Giustino, T. Schmitt, L. C. Duda, M. R. Roberts, P. G. Bruce, *Nat. Chem.* **2018**, *10*, 288.

[8] B. Mortemard de Boisse, S. Nishimura, E. Watanabe, L. Lander, A. Tsuchimoto, J. Kikkawa, E. Kobayashi, D. Asakura, M. Okubo, A. Yamada, *Adv. Energy Mater.* **2018**, *8*, 1800409.

[9] X. Bai, M. Sathiya, B. Mendoza-Sánchez, A. Iadecola, J. Vergnet, R. Dedryvère, M. Saubanère, A. M. Abakumov, P. Rozier, J.-M. Tarascon, *Adv. Energy Mater.* **2018**, *8*, 1802379.

[10] P. E. Pearce, A. J. Perez, G. Rousse, M. Saubanère, D. Batuk, D. Foix, E. McCalla, A. M. Abakumov, G. Van Tendeloo, M.-L. Doublet, J.-M. Tarascon, *Nat. Mater.* **2017**, *16*, 580.

[11] E. McCalla, M. Abakumov Artem, M. Saubanère, D. Foix, J. Berg Erik, G. Rousse, M.-L. Doublet, D. Gonbeau, P. Novák, G. Van Tendeloo, R. Dominko, J.-M. Tarascon, *Science* **2015**, *350*, 1516.

[12] G. Assat, J.-M. Tarascon, *Nat. Energy* **2018**, *3*, 373.

[13] M. Sathiya, G. Rousse, K. Ramesha, C. P. Laisa, H. Vezin, M. T. Sougrati, M.-L. Doublet, D. Foix, D. Gonbeau, W. Walker, A. S. Prakash, M. Ben Hassine, L. Dupont, J.-M. Tarascon, *Nat. Mater.* **2013**, *12*, 827.

[14] Y. J. Wei, K. Nikolowski, S. Y. Zhan, H. Ehrenberg, S. Oswald, G. Chen, C. Z. Wang, H. Chen, *Electrochem. Commun.* **2009**, *11*, 2008.

[15] C. S. Johnson, N. Li, C. Lefief, J. T. Vaughey, M. M. Thackeray, *Chem. Mater.* **2008**, *20*, 6095.

[16] H. Koga, L. Croguennec, M. Ménétrier, P. Mannessiez, F. Weill, C. Delmas, *J. Power Sources* **2013**, *236*, 250.

[17] K. Luo, M. R. Roberts, R. Hao, N. Guerrini, D. M. Pickup, Y.-S. Liu, K. Edström, J. Guo, A. V. Chadwick, L. C. Duda, P. G. Bruce, *Nat. Chem.* **2016**, *8*, 684.

[18] A. J. Naylor, E. Makkos, J. Maibach, N. Guerrini, A. Sobkowiak, E. Björklund, J. G. Lozano, A. S. Menon, R. Younesi, M. R. Roberts, K. Edström, M. S. Islam, P. G. Bruce, *J. Mater. Chem. A* **2019**, *7*, 25355.

[19] J. Xu, M. Sun, R. Qiao, S. E. Renfrew, L. Ma, T. Wu, S. Hwang, D. Nordlund, D. Su, K. Amine, J. Lu, B. D. McCloskey, W. Yang, W. Tong, *Nat. Commun.* **2018**, *9*, 947.

[20] Z. Zhu, D. Yu, Y. Yang, C. Su, Y. Huang, Y. Dong, I. Waluyo, B. Wang, A. Hunt, X. Yao, J. Lee, W. Xue, J. Li, *Nat. Energy* **2019**, *4*, 1049.

[21] M. Tang, A. Dalzini, X. Li, X. Feng, P.-H. Chien, L. Song, Y.-Y. Hu, *J. Phys. Chem. Lett.* **2017**, *8*, 4009.

[22] K. Dai, J. Wu, Z. Zhuo, Q. Li, S. Sallis, J. Mao, G. Ai, C. Sun, Z. Li, W. E. Gent, W. C. Chueh, Y. Chuang, R. Zeng, Z. Shen, F. Pan, S. Yan, L. F. J. Piper, Z. Hussain, G. Liu, W. Yang, *Joule* **2019**, *3*, 518.

[23] W. E. Gent, I. I. Abate, W. Yang, L. F. Nazar, W. C. Chueh, *Joule* **2020**, *4*, 1369.

[24] J. Hong, W. E. Gent, P. Xiao, K. Lim, D.-H. Seo, J. Wu, P. M. Csernica, C. J. Takacs, D. Nordlund, C.-J. Sun, K. H. Stone, D. Passarello, W. Yang, D. Prendergast, G. Ceder, M. F. Toney, W. C. Chueh, *Nat. Mater.* **2019**, *18*, 256.

[25] R. A. House, J.-J. Marie, M. A. Pérez-Osorio, G. J. Rees, E. Boivin, P. G. Bruce, *Nat. Energy* **2021**, *6*, 781.

[26] D.-H. Seo, J. Lee, A. Urban, R. Malik, S. Kang, G. Ceder, *Nat. Chem.* **2016**, *8*, 692.

[27] H. Chen, M. S. Islam, *Chem. Mater.* **2016**, *28*, 6656.

[28] D. A. Kitchaev, J. Vinckeviciute, A. Van der Ven, *J. Am. Chem. Soc.* **2021**, *143*, 1908.

[29] J. Vinckeviciute, D. A. Kitchaev, A. Van der Ven, *Chem. Mater.* **2021**, *33*, 1625.

[30] O. Pecher, J. Carretero-González, K. J. Griffith, C. P. Grey, *Chem. Mater.* **2017**, *29*, 213.

[31] D. M. Halat, R. Dervişoğlu, G. Kim, M. T. Dunstan, F. Blanc, D. S. Middlemiss, C. P. Grey, *J. Am. Chem. Soc.* **2016**, *138*, 11958.

[32] I. D. Seymour, D. S. Middlemiss, D. M. Halat, N. M. Trease, A. J. Pell, C. P. Grey, *J. Am. Chem. Soc.* **2016**, *138*, 9405.

[33] S. Hanashima, N. Fujiwara, K. Matsumoto, N. Iwaski, G. Zheng, H. Torigoe, K. Suzuki, N. Taniguchi, Y. Yamaguchi, *Chem. Commun.* **2013**, *49*, 1449.

[34] X. Kong, V. V. Terskikh, R. L. Khade, L. Yang, A. Rorick, Y. Zhang, P. He, Y. Huang, G. Wu, *Angew. Chem., Int. Ed.* **2015**, *54*, 4753.

[35] M. Wang, X.-P. Wu, S. Zheng, L. Zhao, L. Li, L. Shen, Y. Gao, N. Xue, X. Guo, W. Huang, Z. Gan, F. Blanc, Z. Yu, X. Ke, W. Ding, X.-Q. Gong, C. P. Grey, L. Peng, *Sci. Adv.* **2015**, *1*, e1400133.

[36] F. Geng, B. Hu, C. Li, C. Zhao, O. Lafon, J. Trébosc, J.-P. Amoureux, M. Shen, B. Hu, *J. Mater. Chem. A* **2020**, *8*, 16515.

[37] F. Geng, M. Shen, B. Hu, Y. Liu, L. Zeng, B. Hu, *Chem. Commun.* **2019**, *55*, 7550.

[38] S. Schramm, R. J. Kirkpatrick, E. Oldfield, *J. Am. Chem. Soc.* **1983**, *105*, 2483.

[39] J. Bréger, M. Jiang, N. Dupré, Y. S. Meng, Y. Shao-Horn, G. Ceder, C. P. Grey, *J. Solid State Chem.* **2005**, *178*, 2575.

[40] L. A. O'Dell, R. W. Schurko, *Chem. Phys. Lett.* **2008**, *464*, 97.

[41] A. Boulineau, L. Croguennec, C. Delmas, F. Weill, *Chem. Mater.* **2009**, *21*, 4216.

[42] P. Strobel, B. Lambert-Andron, *J. Solid State Chem.* **1988**, *75*, 90.

[43] D. Y. W. Yu, K. Yanagida, Y. Kato, H. Nakamura, *J. Electrochem. Soc.* **2009**, *156*, A417.

[44] G. G. Amatucci, J. M. Tarascon, L. C. Klein, *J. Electrochem. Soc.* **1996**, *143*, 1114.

[45] C. Pouillerie, L. Croguennec, C. Delmas, *Solid State Ionics* **2000**, *132*, 15.

[46] M. D. Radin, J. Vinckeviciute, R. Seshadri, A. Van der Ven, *Nat. Energy* **2019**, *4*, 639.

[47] R. Xiao, H. Li, L. Chen, *Chem. Mater.* **2012**, *24*, 4242.

[48] P. Yan, L. Xiao, J. Zheng, Y. Zhou, Y. He, X. Zu, S. X. Mao, J. Xiao, F. Gao, J.-G. Zhang, C.-M. Wang, *Chem. Mater.* **2015**, *27*, 975.

[49] E. Adamczyk, V. Pralong, *Chem. Mater.* **2017**, *29*, 4645.

[50] G. Kresse, J. Furthmüller, *Phys. Rev. B* **1996**, *54*, 11169.

[51] G. Kresse, J. Furthmüller, *Comput. Mater. Sci.* **1996**, *6*, 15.

[52] P. E. Blöchl, *Phys. Rev. B* **1994**, *50*, 17953.

[53] G. Kresse, D. Joubert, *Phys. Rev. B* **1999**, *59*, 1758.

[54] J. P. Perdew, K. Burke, M. Ernzerhof, *Phys. Rev. Lett.* **1996**, *77*, 3865.

[55] S. L. Dudarev, G. A. Botton, S. Y. Savrasov, C. J. Humphreys, A. P. Sutton, *Phys. Rev. B* **1998**, *57*, 1505.

[56] A. Jain, G. Hautier, C. J. Moore, S. Ping Ong, C. C. Fischer, T. Mueller, K. A. Persson, G. Ceder, *Comput. Mater. Sci.* **2011**, *50*, 2295.

[57] J. Sun, A. Ruzsinszky, J. P. Perdew, *Phys. Rev. Lett.* **2015**, *115*, 036402.

[58] H. Peng, Z.-H. Yang, J. P. Perdew, J. Sun, *Phys. Rev. X* **2016**, *6*, 041005.

[59] O. Y. Long, G. Sai Gautam, E. A. Carter, *Phys. Rev. Mater.* **2020**, *4*, 045401.

[60] S. P. Ong, W. D. Richards, A. Jain, G. Hautier, M. Kocher, S. Cholia, D. Gunter, V. L. Chevrier, K. A. Persson, G. Ceder, *Comput. Mater. Sci.* **2013**, *68*, 314.

[61] G. L. W. Hart, R. W. Forcade, *Phys. Rev. B* **2008**, *77*, 224115.

[62] G. L. W. Hart, R. W. Forcade, *Phys. Rev. B* **2009**, *80*, 014120.

[63] G. L. W. Hart, L. J. Nelson, R. W. Forcade, *Comput. Mater. Sci.* **2012**, *59*, 101.